

DRAFT

CMS Paper

The content of this note is intended for CMS internal use and distribution only

2012/11/29

Head Id: 159590

Archive Id: 159591

Archive Date: 2012/11/29

Archive Tag: trunk

Measurement of the $W\gamma$ and $Z\gamma$ cross sections and limits on anomalous triple gauge couplings at $\sqrt{s} = 7$ TeV

Draft v.8

The CMS Collaboration

Abstract

Measurements of $W\gamma$ and $Z\gamma$ cross sections in proton-proton collisions at $\sqrt{s} = 7$ TeV are presented and used for extraction of upper limits on anomalous triple gauge couplings. Results are based on data recorded by the CMS experiment at the LHC that correspond to an integrated luminosity of 5 fb^{-1} . The cross sections are measured for photon transverse momenta $p_T^\gamma > 15 \text{ GeV}$ in the $\ell\nu\gamma$ and $\ell\ell\gamma$ final states, where ℓ refers either to an electron or a muon. Limits set on anomalous trilinear $WW\gamma$, $ZZ\gamma$, and $Z\gamma\gamma$ gauge couplings are the most stringent to date.

This box is only visible in draft mode. Please make sure the values below make sense.

PDFAuthor:	A. Barker, O. Bondu, I. Chakaberia, K.-H. Chen, S. Duric, L. Gray, O.H. Hindrichs, S.-W. Li, I. Svintradze, J. Veverka, A. Askew, T. Bolton, A. Bornheim, V. Brigljevic, Y.-H. Chang, S. Dasu, S. Gascon-Shotkin, M. Gataullin, Y. Gershtein, E. Halkiadakis, I. Kravchenko, C.-M. Kuo, A. Lanaro, M. Lethuillier, W.-T. Lin, Y. Maravin, H. Newman, F. Raupach, J. Reichert
PDFTitle:	Measurement of the W-gamma and Z-gamma Cross Sections and Limits on Anomalous Triple Gauge Couplings at sqrt-s = 7 TeV
PDFSubject:	CMS
PDFKeywords:	CMS, physics, software, computing

Please also verify that the abstract does not use any user defined symbols

1 This document is a draft of the final paper, targeted for PRD, and will be updated during review with an
 2 ARC. The full information about these analyses can be found in AN-11-251.

3 1 Introduction

4 A precise measurement of the pair production of electroweak bosons provides direct informa-
 5 tion on trilinear gauge couplings (TGC), the least well-measured couplings of the electroweak
 6 sector of the standard model (SM). The self-interactions predicted among the gauge bosons in
 7 the SM determine all possible TGC, and any deviation from these values would be indicative
 8 of the presence of new physics. Electroweak measurements at LEP [1–4], the Tevatron [5–
 9 10], and the LHC [11–13] have already explored some of the parameter space of anomalous
 10 TGC (aTGC). Previous results from LHC are limited by insufficient statistics of the data, and
 11 a significant improvement in precision of TGC measurements at LHC energies is expected at
 12 7 and 8 TeV. Extensions of the SM predict additional processes with multiple bosons in the fi-
 13 nal state. If such phenomena contribute at large energy scales, i.e. beyond the mass reach of
 14 LHC, nevertheless causes changes in TGC. Precise measurements of diboson properties and
 15 their cross sections, therefore, also crucial for correct interpretation of production of Higgs-like
 16 bosons at the LHC and their primary backgrounds. Among the electroweak diboson produc-
 17 tion processes at hadron colliders, $W\gamma$ and $Z\gamma$ final states have the highest yields, next to $\gamma\gamma$
 18 production. Background processes to $W\gamma$ and $Z\gamma$ are significantly suppressed as a result of the
 19 ability to identify heavy vector bosons. Hence, these processes are optimal for measuring TGC
 20 and checking thereby the SM description of the electroweak sector of the LHC.

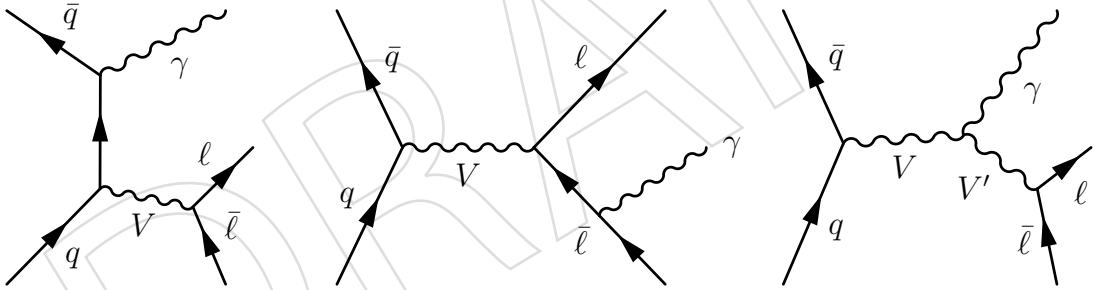


Figure 1: Feynman diagrams of $V\gamma$ production, with V and V' corresponding to both virtual and real γ , W , and Z bosons. The three diagrams reflect contributions from (a) initial-state and (b) final state radiation, and (c) TGC. The TGC diagram does not contribute at the lowest order to $Z\gamma$ production as photons do not couple to particles without electric charge.

21 This paper describes the analysis of inclusive $W\gamma+X$ and $Z\gamma+X$ events, collectively referred
 22 to as “ $V\gamma + X$ ” production, using leptonic decays of the V : $W \rightarrow e\nu$, $W \rightarrow \mu\nu$, $Z \rightarrow ee$, and
 23 $Z \rightarrow \mu\mu$ observed in pp collisions at center-of-mass energy 7 TeV, in data corresponding to 5
 24 fb^{-1} of integrated luminosity. $V\gamma$ production at the lowest “tree” level in electroweak theory
 25 can be represented by the Feynman diagrams of Fig. 1. Three processes contribute: (a) initial
 26 state radiation, where a photon is radiated by one of the incoming virtual partons, (b) final
 27 state radiation, where a photon is radiated off one of the charged leptons from V decay, and (c)
 28 TGC of $WW\gamma$ for $W\gamma$ production, and of $ZZ\gamma$ and $Z\gamma\gamma$ for $Z\gamma$ production. In the SM, the TGC
 29 process is allowed only for $W\gamma$ production, as there are no neutral TGC contributions at three
 30 level.

The production cross section for each $W\gamma$ channel at next-to-leading order is 31.18 ± 1.8 pb [14] for photon transverse momenta > 15 GeV and the angular separation between the charged lepton and photon, ΔR , be larger than 0.7. The equivalent production cross section for each of the $Z\gamma$ channels is 5.45 ± 0.27 pb.

2 CMS Detector and Simulations

The central feature of the CMS apparatus is a superconducting solenoid, 13 m in length and 6 m in diameter, which provides an axial magnetic field of 3.8 T. The bore of the solenoid is instrumented with particle detection systems that provide excellent performance for the reconstruction and identification of muons, electrons, and photons. Charged particle trajectories are measured with silicon pixel and strip trackers, covering $0 < \phi < 2\pi$ in azimuthal angle and $|\eta| < 2.5$, where the pseudorapidity η is defined as $\eta = -\ln[\tan \theta/2]$, with θ being the polar angle of the trajectory of the particle with respect to counterclockwise beam direction. A lead tungstate crystal electromagnetic calorimeter (ECAL) and a brass/scintillator hadronic calorimeter (HCAL) surround the tracking volume. The good spatial and momentum resolution of the ECAL provides precise measurements of electrons and photons, which are crucial to this analysis. Muons are identified and measured in gas detectors embedded in the steel return yoke outside of the solenoid. The detector is nearly hermetic, providing thereby accurate measurements of the imbalance in momentum in the plane transverse to the beam directions (\cancel{E}_T). A two-tier trigger system selects the most interesting pp collision events for use in analyses. A more detailed description of the CMS detector can be found in Ref. [15].

The main background to $W\gamma$ and $Z\gamma$ production consists of W +jets and Z +jets events, respectively, in cases when one of the jets is mis-identified as a photon. We estimate this background using data to minimize systematic uncertainties associated with modeling of jet fragmentation in Monte Carlo (MC) simulation. The contributions from other processes, such as $t\bar{t}$, γ +jets and multijet production, are two orders of magnitude smaller and are estimated from MC simulation.

All signal MC samples for $W\gamma + n$ jets and $Z\gamma + n$ jets with $n < 3$ are generated with MADGRAPH5 [16], interfaced to PYTHIA [17] for showering, hadronization, and matching of jets to original partons. The kinematic distributions for these processes are cross-checked with expectations from SHERPA [18] and the predictions from the two programs are found in agreement. The signal samples are normalized using next-to-leading order (NLO) predictions from the MCFM generator [14]. Background processes are simulated with the MADGRAPH interfaced to PYTHIA for $t\bar{t}$, W +jets, and Z +jets events. Multijet, γ +jets, and diboson processes are generated using the PYTHIA MC program but have negligible impact on the final selected sample. All simulated samples are generated with leading order (LO) parton distribution functions (PDF) [19], and events are passed through a detailed simulation of the CMS detector based on GEANT4 [20], and reconstructed with chain of programs used for data.

3 Selection of Candidate Events

In this section we document the selection criteria used to select the events and to identify the final-state leptons and photons. Although almost all selections criteria are corrected for the effects from the presence of pileup (PU) in interactions, we will present the effectiveness of the selection criteria separately for the low and high-PU sets of data. There is an average of 4.9 interactions per collision for low-PU data and on average of 7.8 interactions for high-PU data

corresponding, respectively to about 2.2 fb^{-1} (referred to as 2011A in the text) and to $\sim 2.7 \text{ fb}^{-1}$ (referred to as 2011B data) of integrated luminosity.

3.1 Trigger Requirements

The $W\gamma \rightarrow \ell\nu\gamma$ and $Z\gamma \rightarrow \ell\ell\gamma$ events are selected using unprescaled isolated lepton triggers with lowest available p_T thresholds. These thresholds and the trigger-level isolation requirements on lepton candidates evolved during the run to accommodate rising instantaneous luminosity and are less stringent than the off-line requirements.

The trigger considers electron candidates in rapidity range $|\eta_e| < 3$. For $W\gamma \rightarrow \ell\nu\gamma$ channel, an isolated single electron trigger with a threshold of 32 GeV is used, except for the first 0.2 fb^{-1} of Run 2011A where the threshold is 27 GeV. In addition, for the last 1.9 fb^{-1} of Run 2011A and entire 2011B an additional requirement on the transverse mass M_T^W of the electron candidate and the missing transverse energy (\cancel{E}_T) defined as $M_T^W = \sqrt{2 \times p_T(\ell) \times \cancel{E}_T \times (1 - \cos \Delta\phi(\ell, \cancel{E}_T))} > 50 \text{ GeV}$ is made.

The $Z\gamma \rightarrow ee\gamma$ process makes use of a trigger requiring two isolated electron candidates with p_T thresholds of 17 GeV on the leading and 8 GeV on the trailing candidate.

The trigger for $W\gamma \rightarrow \mu\nu\gamma$ events requires an isolated muon with p_T above 30 GeV and $|\eta| < 2.4(2.1)$ for Run 2011A (2011B).

The dimuon trigger used to collect $Z\gamma \rightarrow \mu\mu\gamma$ events does not require these muons to be isolated. For most of the data, the muon p_T thresholds are 13 GeV for the leading and 8 GeV for the trailing candidates. These thresholds were 7 and 7 GeV for the first 0.2 fb^{-1} of Run 2011A, and 17 and 8 GeV for the last 0.8 fb^{-1} of Run 2011B.

3.2 Muon Identification and Selection

Muons are reconstructed offline by matching trajectories from the inner tracker and the outer muon systems. We use the muon identification scheme defined in Ref. [21], with minor changes to requirements on the distance of closest approach of the muon track to the primary vertex in the longitudinal direction (z): $|d_z| < 0.1 \text{ cm}$, and the distance of closest approach in the transverse plane: $|d_0| < 0.02 \text{ cm}$.

The efficiencies of these criteria are measured in data and in MC simulation using the $Z \rightarrow \ell\ell$ events and the tag-and-probe technique. A small correction of the order of 3% is applied to the MC simulation to match the performance in data.

3.3 Electron Identification and Selection

Electrons are identified as clusters of energy deposits, so-called super clusters (SC)[22], in the ECAL fiducial volume spatially matched to tracks from the silicon tracker. The SC are required to be identified inside the tracker acceptance with $|\eta| < 2.5$. The ECAL region of reduced longitudinal shower containment between barrel and endcap sections of the calorimeter with $1.4442 < |\eta| < 1.566$ is also excluded.

The width of the SC in η is described by the quantity $\sigma_{i\eta i\eta}$ defined in Ref.[22]. We require this width to be narrow, consistent with the profile of the electromagnetic shower.

We require reconstructed electron tracks to be of good quality with no missing hits associated to the track. We also require the charged track to be inconsistent with early photon conversion hypothesis by rejecting candidates that have a partner track that is close to the electron candidate's track in distance $|\text{dist}|$ and angle $|\cot \Delta\theta|$. The electron candidate is required to have a

transverse momentum $p_T > 35$ and 20 GeV for $W\gamma$ and $Z\gamma$ analyses, respectively. To ensure that the selected electron candidate is consistent with being produced from the primary interaction vertex in the event, the distance of closest approach to the z-axis must be below 0.1 cm. The separation of the z-coordinate of the primary vertex of the event from the z-coordinate of the point of electron candidate's closest approach to z-axis must not be larger than 0.02 cm.

To reduce the background from misidentified jets, we require electron candidates to be isolated from other activity in the detector. The relative isolation of the electron candidate is calculated by determining separately the sum of track momentum, ECAL, and HCAL energy deposits not associated with the electron candidate in the spatial cone of $\Delta R = \sqrt{\Delta\phi^2 + \Delta\eta^2} = 0.3$ and normalizing it to the electron candidate's p_T . In $W\gamma$ analysis we require individual sums from sub-detectors not to exceed optimized thresholds to maximally reject background from misidentified jets at a given efficiency of the selection criteria. We also require the total HCAL energy in $\Delta R = 0.15$ cone around the seed cluster not to exceed 2.5% of the ECAL energy in the same area ($H/E < 0.025$).

In this study we use several sets of criteria with different selection efficiencies, that we refer below as working points (WP) and list in Table 1.

Table 1: Selection criteria for the WP60, WP80, WP85 and WP95 electron candidates in Barrel and Endcap sections of the calorimeter.

channel	WP95		WP85		WP60	
	PU corrected		PU corrected		not PU corrected	
	e veto in $W\gamma$		$Z\gamma$		$W\gamma$	
	Barrel	Endcap	Barrel	Endcap	Barrel	Endcap
$\Delta\phi_{in}$	0.8	0.7	0.039	0.028	0.025	0.02
$\Delta\eta_{in}$	0.007	0.011	0.005	0.007	0.004	0.005
H/E	—	—	—	—	0.025	0.025
$ \cot\Delta\theta $	—	—	0.02	0.02	0.02	0.02
$ \text{dist} $	—	—	0.02	0.02	0.02	0.02
σ_{ijij}	0.012	0.031	0.01	0.031	0.01	0.03
Combined relative isolation	0.15	0.1	0.053	0.042	—	—
Relative ECAL isolation	—	—	—	—	0.04	0.02
Relative HCAL isolation	—	—	—	—	0.03	0.02
Relative TRACKER isolation	—	—	—	—	0.04	0.025

The efficiencies of these criteria are measured in data and in MC simulation using the $Z \rightarrow \ell\ell$ events and the tag-and-probe technique. A small correction of the order of 3% is applied to the MC simulation to match the performance in data.

The electron candidates in MC simulations are weighted by the ratio of efficiency measured using tag-and-probe technique in data to that in MC simulation for $Z \rightarrow ee$ events to reduce systematic uncertainties associated with modeling of electrons in simulation. The MC matches the data well and the ratio does not deviate from one by more than 3%.

3.4 Photon Identification and Selection

Photon candidates are reconstructed as SC with $p_T^\gamma > 15$ GeV in the fiducial volume of the ECAL detector. The efficiency of reconstructing a SC from a photon electromagnetic deposit in the ECAL is measured in MC simulation and is found to be very close to 100%. The photon energy scale is measured using $Z \rightarrow \mu\mu\gamma$ events as described in Appendix A.

Similarly to the 2010 CMS analysis of the $V\gamma$ final states [12], we greatly reduce the rate of jets reconstructed as photons by requiring stringent photon identification criteria, including isolation and shower shape requirements described below:

- Ratio of HCAL to ECAL energies in a cone size of $\Delta R = 0.15$ around the seed crystal must be below 0.05.
- $\sigma_{i\eta i\eta}$ must be below 0.011 in barrel and below 0.030 in endcap,
- photon candidate must have no associated track in the pixel detector to reduce the background from misidentified electrons.

However, unlike the previous analysis, the high pile-up conditions during the 2011 LHC run require alterations to the photon isolation criteria to ensure the robustness of the selection against PU modeling in simulation. The sum of all the tracks' transverse momenta found in the annulus of $0.05 < \Delta R < 0.4$, I_{TRK} , around the photon candidate should not exceed $2 \text{ GeV} + 0.001 \times p_T^\gamma + A_{\text{eff}} \times \rho$, where ρ is the mean background energy density per unit area and computed using FASTJET package [23], and A_{eff} is an effective area correction to ensure the isolation requirement not to exhibit a pile-up dependence. The photon candidate is also required to be isolated in the ECAL by summing the transverse energy deposited in the ECAL in an annulus $0.06 < \Delta R < 0.40$, excluding a rectangular strip of $\Delta\eta \times \Delta\phi = 0.04 \times 0.40$ to reduce the effect of counting the fragments of the converted photon shower. The ECAL isolation, I_{ECAL} , is required to be less than $4.2 \text{ GeV} + 0.006 \times p_T^\gamma + A_{\text{eff}} \times \rho$. Finally we require the HCAL isolation, I_{HCAL} , to be below $2.2 \text{ GeV} + 0.0025 \times p_T^\gamma + A_{\text{eff}} \times \rho$. The values of A_{eff} are tabulated for all three isolation criteria separately for barrel and endcap in Table 2.

Table 2: A_{eff} used for PU correction for photon selection for barrel and endcap, respectively.

Isolation	barrel	endcap
Tracker (I_{TRK})	0.0167	0.032
ECAL (I_{ECAL})	0.183	0.090
HCAL (I_{HCAL})	0.062	0.180

We cross check that the photons are simulated well in MC simulation by comparing the performance of the full photon selection criteria without pixel veto requirements on electrons from Z boson decay. To perform this comparison we require one of the electrons from Z boson decay to pass stringent electron requirements, and check if the other electron satisfy the photon selection criteria with the exception of the requirement of no pixel track.

The efficiency of the requirement of the pixel track veto is calculated using photons from the final state radiation $Z \rightarrow \mu\mu\gamma$ events. The purity of photon candidates in this process is estimated to exceed 99.6% and thus, it is the preferred source of photons that we use to further cross check the efficiency of photon identification criteria and to infer the photon energy scale and resolution. We found that the requirement of no pixel track in data is 97% and 89% efficient in barrel and endcap, respectively.

To estimate the efficiency of the shower shape and isolation requirements with good statistical precision we exploit the similarity between photons and electrons (see Fig. 2) and use tag-and-probe technique with $Z \rightarrow ee$ events. The pixel track veto is not applied for the tag-and-probe study. The ratio of the efficiencies for selecting photons and electrons is also shown in Fig. 2.

We also found that the selection criteria in data and MC simulation agree to better than 3% accuracy in both transverse momentum and pseudorapidity dependence, shown in Fig. 3. Similarly to electrons and muons, we re-weight the simulation events to reduce the residual simulation modeling discrepancy.

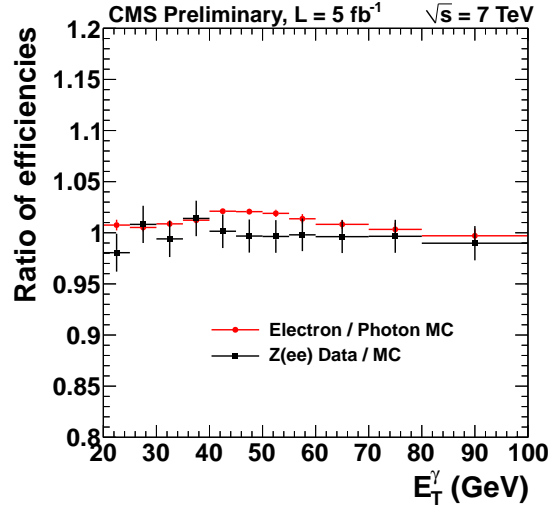


Figure 2: Ratio of photon selection efficiencies using electron tag-and-probe in data and MC simulation (black) and the ratio of MC truth photon efficiencies to MC truth electron efficiencies using photon selection criteria (red) as a function of the photon transverse energy.

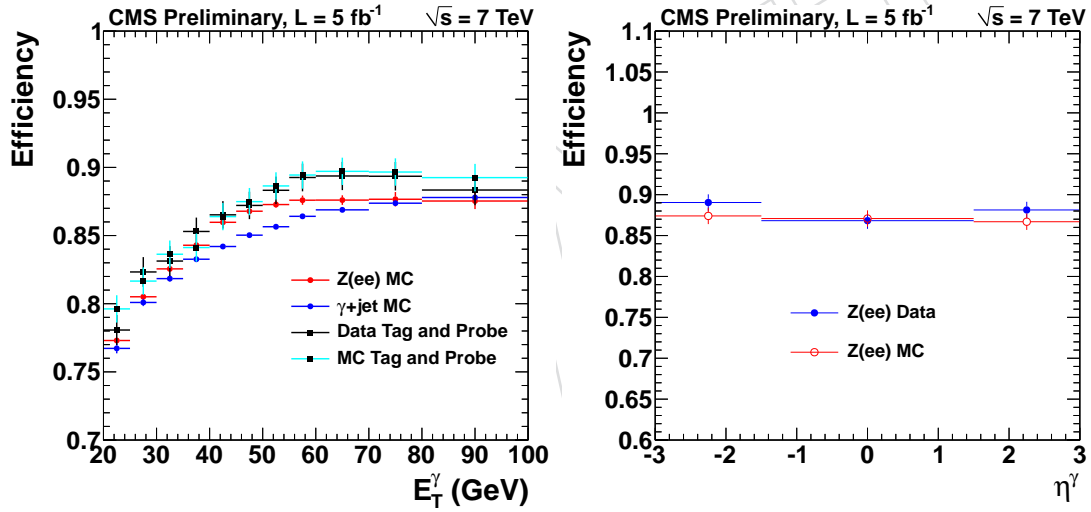


Figure 3: Efficiency of photon selection criteria as a function of photon transverse momentum (left) and pseudorapidity (right).

3.5 Reconstruction of E_T

Neutrino from W decay is not detected directly, but gives rise to an imbalance in transverse momentum E_T . This quantity is computed using the Particle Flow (PF) algorithm [24] that generates a list of four-vectors of reconstructed particles based on the information from all subsystems of the CMS detector. The E_T for each event is then defined by the modulus of the vector sum of the transverse momenta of all reconstructed particles in each event.

3.6 $W\gamma$ Event Selection

The $W\gamma \rightarrow \ell\nu\gamma$ process is characterized by a prompt, energetic, and isolated lepton, a prompt isolated photon, and significant missing energy due to the neutrino.

Both electrons and muons are required to have $p_T > 35$ GeV and the photons are required to have $p_T > 15$ GeV. The maximum allowed $|\eta|$ values for muons, electrons, and photons are 2.1, 2.5, and 3.0 respectively. We require that the photon is separated from the lepton by imposing a cut $\Delta R(\ell, \gamma) > 0.7$. We reject events that have a second reconstructed lepton of the same flavor to remove the contribution from $Z\gamma \rightarrow \ell\ell\gamma$ process. For this veto, electrons are required to have $p_T > 20$ GeV, $|\eta| < 2.5$, and pass WP95 selection (see Table 1), while the muons are required to have $p_T > 10$ GeV, $|\eta| < 2.4$.

To suppress backgrounds without true E_T the transverse mass cut of 70 GeV is imposed. We find that the simulation models the E_T quite adequately (at the level of 4%), and we apply corrections to reduce residual disagreement. The efficiency of the M_T^W selection in data and simulation agree at the level of 2%.

After the full $e\nu\gamma$ selection 7470 events are selected in the data, and 10809 events are selected in the $\mu\nu\gamma$ channel.

3.7 $Z\gamma$ Event Selection

The process is characterized by two prompt, energetic, and isolated leptons and an isolated prompt photon. Both electrons and muons are required to have $p_T > 20$ GeV and the photons are required to have $p_T > 15$ GeV. The maximum allowed $|\eta|$ values for muons, electrons, and photons are 2.4, 2.5, and 3.0 respectively. We require that the photon is separated from the leptons by imposing a cut $\Delta R(\ell, \gamma) > 0.7$. The invariant mass of the leptons is required to be above 50 GeV.

Applying the selection criteria yields 4108 $Z\gamma \rightarrow ee\gamma$ and 6463 $Z\gamma \rightarrow \mu\mu\gamma$ candidate events.

4 Background Estimates

The dominant background for both $W\gamma$ and $Z\gamma$ comes from events with misidentified photons, mostly originating from the jets in W + jets events and Z + jets events, respectively. We estimate the background from these sources in data, using two methods described in Sec. 4.1

For the $W\gamma$ channel the second major background is from Drell–Yan and di-boson production process with an electron and at least one more lepton in the final state, with the former misidentified as photon. This background is estimated from data as described in Sec. 4.2.

Other background to $V\gamma$ process are from

- Misidentified leptons from γ +jet production,
- $V\gamma$ with V decays into τ that decays leptonically,
- $t\bar{t}\gamma$ events,
- $Z\gamma$ events where one of the leptons from Z decays is not reconstructed

All these backgrounds are estimated to be small compared to the V + jets contribution and are estimated from MC simulation.

4.1 Jets misidentified as photons

4.1.1 The Template Method

The template method uses the $\sigma_{i\eta j\eta}$ distribution to determine the number of genuine photons from misidentified jets passing full selection criteria by performing a two-component extended

maximum log-likelihood fit of signal and background $\sigma_{i\eta i\eta}$ templates to data.

The signal shape is obtained from photon candidates in simulation. We cross check the simulation of electromagnetic shower in MC and data using $Z \rightarrow ee$ events. Events are required to have at least two electron candidates with $p_T > 20$ GeV and pass WP80 selection criteria described in Sec. 3.3 but without $\sigma_{i\eta i\eta}$ requirement. Both electron candidates must be identified in the ECAL fiducial volume and have invariant mass between 60 and 120 GeV. One of the electron candidates, a tag, is required to pass the tight trigger criteria of the di-electron trigger, while no trigger requirements are applied on the other electron candidate, a probe. The purity of this selection is estimated to be 99% for both barrel and endcap regions.

The background templates were made from jet-enriched data. Photon candidates in these events are required to pass the photon selection criteria described in Sec. 3.4, except for the $\sigma_{i\eta i\eta}$ requirement and I_{TRK} which is required to be within the following range:

- $2 \text{ GeV} < I_{\text{TRK}} - 0.001 \times E_T^\gamma - 0.0167 \times \rho < 5 \text{ GeV}$ for $|\eta_\gamma| < 1.4442$
- $2 \text{ GeV} < I_{\text{TRK}} - 0.001 \times E_T^\gamma - 0.0320 \times \rho < 3 \text{ GeV}$ for $1.560 < |\eta_\gamma| < 2.5$

This requirement ensures that the contribution from genuine photons is negligible, and keeping the isolation requirements close to those for photon selection criteria allows selecting jets with large electromagnetic fraction that have properties similar to those of genuine photons. We also observe that in simulated jet events the $\sigma_{i\eta i\eta}$ is found largely uncorrelated with isolation requirement, so the background shape observed for photon-like jets with the inverted tracker isolation should be the same as that for isolated photon-like jets.

We investigated a possible correlation between the shape of the $\sigma_{i\eta i\eta}$ template for background the presence of \cancel{E}_T parallel with the photon-like jet. Since the M_T^W requirement is used in $W\gamma$ selection, a presence of \cancel{E}_T in the event can bias the background template and affect the background estimate. To estimate this effect we re-derived the background $\sigma_{i\eta i\eta}$ templates for events where $\cancel{E}_T > 10$ GeV and \cancel{E}_T is parallel to the direction of the photon-like jet. We estimate the systematic uncertainty using the lowest E_T^γ bin only, as this is the bin providing the largest background yield, and thus, is the largest control sample from which to derive the background template. Using the new templates we assigned the systematic uncertainty to be the largest disagreement from the nominal yield and found it to be 13% and 7% for barrel and endcap, respectively.

The systematic uncertainty on the electron misidentification is estimated by varying the fit models, electron and photon energy resolution, and pile-up distributions in MC simulation.

The $\sigma_{i\eta i\eta}$ distribution in data are fit to

$$f(\sigma_{i\eta i\eta}) = N_S S(\sigma_{i\eta i\eta}) + N_B B(\sigma_{i\eta i\eta}), \quad (1)$$

where N_S and N_B are the expected number of signal and background candidates. $S(\sigma_{i\eta i\eta})$ and $B(\sigma_{i\eta i\eta})$ are the signal and background component templates. The template data are smoothed using kernel density estimation [25] or direct interpolation, in the case of high template statistics. This allows for unbinned fits of the $\sigma_{i\eta i\eta}$ distribution of selected photons to be performed, preserving performance of the fit in low statistics scenarios.

The fit is performed by using a unbinned extended maximum likelihood, by minimizing:

$$-\ln L = (N_S + N_B) - N \ln(N_S S(\sigma_{i\eta i\eta}) + N_B B(\sigma_{i\eta i\eta})). \quad (2)$$

where N is the total number of data events in the given p_T bin.

4.1.2 The Ratio Method

We use a second method referred to as the 'ratio method' to infer the $V + \text{jets}$ background as a cross-check to the results of the template method at high p_T^γ where the template method is subject to larger statistical uncertainties. This method takes advantage of the relatively high statistics in $\gamma + \text{jets}$ data sample and the expected similarity between the misidentification rate for jets in $\gamma + \text{jets}$ sample and $V\gamma$ data. Thus, this method can provide a higher precision estimate of the $V + \text{jet}$ background at large p_T^γ .

This method exploits a category of jets that have similar properties to electromagnetic objects in the ECAL; these jets are called photon-like jets. Photon-like jets are selected by identifying a reconstructed photon which fails the photon isolation or $\sigma_{i\eta i\eta}$ requirements of final photon selection, but are more isolated and have a higher electromagnetic fraction than most hadronic jets. The ratio method measures the ratio R_p of the probability of a jet to pass the photon-like jet requirements to that of passing the final photon selection criteria. Once R_p is known, the number of jets that satisfy the final photon selection criteria $N_{V+\text{jets}}$ can be estimated as the product of R_p and the number of photon-like jets counted in data.

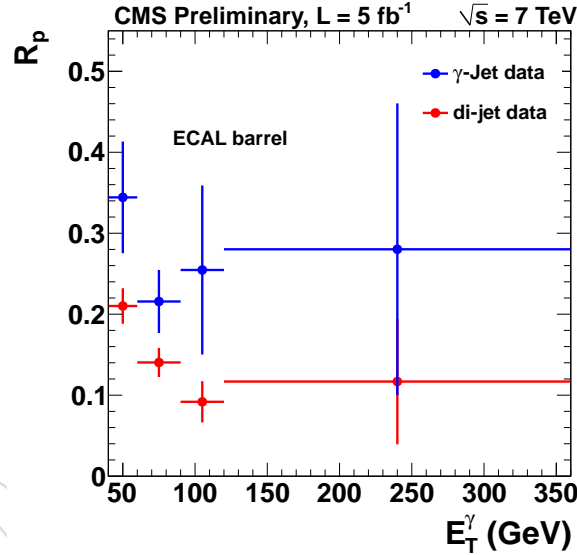


Figure 4: R_p as a function a photon candidate p_T for barrel ECAL in $\gamma + \text{jet}$ and multijet QCD samples. The difference in R_p values between two processes is due to the fact that jets in the former process are dominated by quark fragmentation, while that in the latter process are dominated by gluon fragmentation.

We measure R_p for each p_T^γ bin of the analyses separately for the ECAL barrel and endcaps. R_p is determined using a di-photon sample defined by either two photon candidates passing the final selection or one photon candidate passing final selection and one passing photon-like jet selection. To reduce correlations induced by the di-photon kinematics we require that the photons of each di-photon candidate in either category be in the same η region and p_T^γ bin. A two-dimensional template fit of $\sigma_{i\eta i\eta}$ distributions of each photon candidates in the di-photon system is performed to estimate R_p to estimate and remove the contribution from genuine photons to the photon-like jet yield. A correction factor $\alpha \approx 5 - 10\%$ is applied to account for the case where genuine photons satisfy photon-like jet definitions. The correction is derived from simulation and checked using $Z \rightarrow ee$ data and simulation.

The observed R_p values for the ECAL barrel are given in Fig. 4. The difference between R_p

values measured in different processes demonstrate the sensitivity of the method to the flavor of the jet. We use W+jet and Z+jet simulation to estimate gluon-to-quark ratio and correct the R_p measured in data. We find the predictions of the ratio method to be consistent with the ones of the template method, and consider the difference between them as an extra source of systematic uncertainty.

4.2 Background From Electrons Misidentified as Photons to $W\gamma \rightarrow \ell\nu\gamma$

The criterion that allows separating electrons from photons is the requirement of no pixel track associated with the photon candidate. We measure the probability P for an electron to have no pixel track match in $Z \rightarrow ee$ data sample, by requiring one of the electrons to pass stringent electron identification criteria and checking how often the other electrons pass the full photon selection criteria including the requirement of no associated pixel track. Fitting the di-electron invariant mass distribution by a convolution of a Breit-Wigner and Crystal Ball function to describe the signal and an exponential decay for background we obtained the efficiency of an electron to have no associated pixel track to be 0.014 ± 0.003 for barrel and 0.028 ± 0.004 for endcap. Then, to estimate the background from electron misidentification in $W\gamma \rightarrow \mu\nu\gamma$ channel, we select the events that pass the full selection criteria, except for the photon candidate that is required to pass photon selection criteria but the pixel track match. Then the contribution from genuine electrons misidentified as photons can be calculated from

$$N_{e \rightarrow \gamma} = N_{\mu\nu e} \times \frac{P}{1-P} \quad (3)$$

where $N_{e \rightarrow \gamma}$ is the background from the misidentified electrons, and $N_{\mu\nu e}$ is the number of events selected without the requirement of the pixel track match. We found this background for muon channel to be 91.4 ± 1.4 (stat.) ± 4.7 (syst.).

For the electron channel, we separate contributions from Z + jets and W + jets, $t\bar{t}$ + jets, and others. The contribution from the former is estimated by applying full $W\gamma \rightarrow e\nu\gamma$ selection criteria.

Then the invariant mass of a photon and an electron candidates are fit to the Breit-Wigner convoluted with the Crystal Ball function for signal and an exponential decay function for background to estimate the contribution from $Z/\gamma^* \rightarrow ee$ process. We find the contribution from $Z/\gamma^* \rightarrow ee$ process to be 620.1 ± 19.4 (stat.) ± 48.6 (syst.).

Contributions from other sources with genuine electrons misidentified as photons from W + jets, $t\bar{t}$ + jets, and diboson processes are estimated using MC simulation, where a photon candidate is spatially matched to the generator-level electrons. We estimate the contribution from these sources to be 69.1 ± 6.7 (stat.) ± 7.3 (syst.).

4.3 Total Background

4.3.1 $\ell\nu\gamma$ events

The jet-photon misidentification background is summarize in Table 3 for different photon p_T bins. Total background is shown in Table 4.

need numbers in table 3 for the ratio method

A comparison of the E_T^γ distributions between data and Monte Carlo simulation after the full event selection is shown in Fig. 5 for the muon and electrons channels.

Photon p_T , GeV	W+jet yield	photon shape	jet shape	sampling of the distributions	photon - \cancel{E}_T correlation	diff. with ratio method
Barrel + Endcap: $ev\gamma / \mu\nu\gamma$						
15-20	1452.3 / 2762.9	9.3 / 20.5	83.2 / 59.4	19.2 / 35.6	129.1 / 251.7	-
20-25	648.4 / 1108.3	5.2 / 19.5	37.0 / 33.8	11.2 / 18.8	54.4 / 94.2	-
25-30	365.3 / 521.6	3.7 / 9.4	21.0 / 20.7	9.4 / 14.2	32.7 / 43.0	-
30-35	214.9 / 326.3	10.5 / 3.3	12.3 / 16.9	7.5 / 11.1	19.0 / 29.3	-
35-40	156.6 / 194.8	3.4 / 2.8	10.1 / 11.4	6.2 / 7.9	13.7 / 16.1	-
40-60	221.4 / 272.3	3.5 / 0.7	18.8 / 23.4	5.1 / 6.3	19.2 / 24.0	22.1 / 4.4
60-90	77.2 / 100.5	1.4 / 0.9	10.2 / 13.3	3.0 / 3.8	6.6 / 8.5	7.7 / 1.6
90-120	25.7 / 21.4	2.0 / 2.3	5.3 / 4.1	0.9 / 0.9	2.4 / 1.8	2.6 / 0.4
120-500	14.8 / 38.1	4.3 / 2.1	7.6 / 25.9	1.1 / 0.7	1.0 / 3.9	1.5 / 0.6
Total	3176.5 / 5345.9	16.9 / 30.3	97.6 / 83.3	26.7 / 45.4	277.8 / 472.1	33.9 / 7.0
310.4 / 482.6						

Table 3: Uncertainties on the W+jet background estimate for $W\gamma \rightarrow \ell\nu\gamma$ by the template method.

Parameter	$ev\gamma$	$\mu\nu\gamma$
N_{obs}	7470.0	10809
$N_{\text{bkg}}^{W+\text{jets}}$	3176.5 ± 46.8 (stat.) ± 310.4 (syst.)	5345.9 ± 58.2 (stat.) ± 482.6 (syst.)
$N_{\text{bkg}}^{ee\bar{X}}$	689.2 ± 20.5 (stat.) ± 49.1 (syst.)	91.4 ± 1.4 (stat.) ± 4.7 (syst.)
$N_{\text{bkg}}^{\text{other}}$	405.2 ± 18.0 (stat.) ± 25.2 (syst.)	402.8 ± 18.6 (stat.) ± 27.2 (syst.)
N_{Sig}	3199.1 ± 102.0 (stat.) ± 323.0 (syst.)	4968.9 ± 120.6 (stat.) ± 505.8 (syst.)
$A \cdot \epsilon_{MC, W\gamma \rightarrow \ell\nu\gamma}$	0.0187 ± 0.0010 (syst.)	0.0270 ± 0.0014 (syst.)
ρ_{eff}	0.9400 ± 0.0273 (syst.)	0.9898 ± 0.0247 (syst.)
$\int \mathcal{L} dt$	5.0 ± 0.1 (syst.)	5.0 ± 0.1 (syst.)

Table 4: Summary of parameters for the $W\gamma \rightarrow ev\gamma$ and $W\gamma \rightarrow \mu\nu\gamma$ cross section measurements.

Fig. 6 shows the charged-signed η distribution of $W\gamma$ events and demonstrates the radiation amplitude zero characteristic of $W\gamma$ production; these events were selected vetoing events with jets greater than 30 GeV and events with $M_T^{3l} < 110$ GeV.

4.3.2 $\ell\ell\gamma$ events

The jet-photon misidentification background is summarize in Table 5 The other backgrounds from QCD multijet, photon+jets, $t\bar{t}$, and other di-boson processes are estimated from simulation to contribute 38.3 ± 2.8 and 23.7 ± 2.2 events for $ee\gamma$ and $\mu\mu\gamma$ channels, respectively.

numbers disagree with table

The E_T^γ distributions for data and MC simulation, after applying full selection criteria, are shown in Fig. 7, for the $ee\gamma$ and $\mu\mu\gamma$ final states.

5 Production Cross Section Measurements

The measurement of the cross section is given canonically by the formula:

$$\sigma = \frac{N_{\text{sig}}}{A_{\ell\nu\gamma(\ell\ell\gamma)} \cdot \epsilon \cdot \mathcal{L}} \quad (4)$$

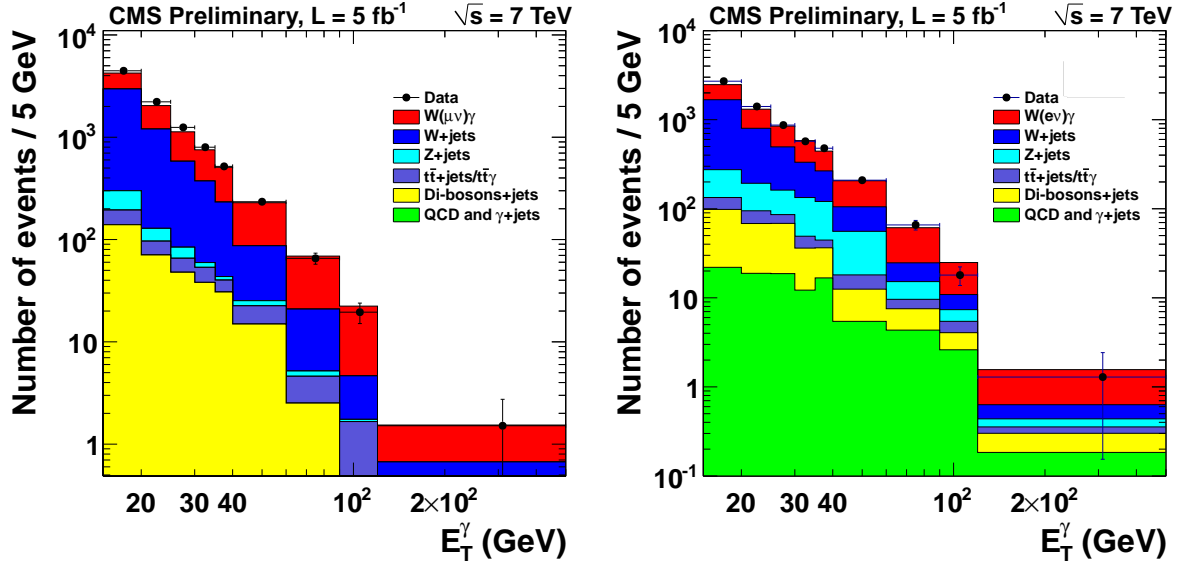


Figure 5: Photon candidate E_T^γ distributions of the $W\gamma$ candidates in data, signal and background MC simulation for $W\gamma \rightarrow \mu\nu\gamma$ (left) and $W\gamma \rightarrow e\nu\gamma$ (right).

Photon E_T , GeV	Mean background yield	Systematic from signal shape	Systematic from background shape	Systematic from sampling of the distribution	Systematic from Δ (Ratio V.S. Template)
Barrel + Endcap $ee\gamma / \mu\mu\gamma$					
15-20	464.9 / 712.1	11.1 / 49.7	26.7 / 41.0	6.4 / 16.0	n/a
20-25	199.2 / 305.9	6.8 / 22.7	11.4 / 17.5	3.7 / 6.7	n/a
25-30	81.8 / 133.2	3.7 / 7.6	4.7 / 7.6	2.3 / 3.0	n/a
30-35	50.5 / 81.6	2.8 / 10.0	2.9 / 4.7	1.9 / 1.8	n/a
35-40	45.5 / 53.7	3.0 / 4.0	2.6 / 3.6	1.8 / 1.2	n/a
40-60	40.4 / 72.3	3.8 / 10.5	2.3 / 5.8	0.9 / 1.5	10.5 / 9.5
60-90	18.3 / 25.2	3.0 / 6.5	1.1 / 3.6	0.7 / 0.6	4.8 / 3.2
90-120	0.0 / 13.9	0.0 / 3.8	0.0 / 1.9	0.0 / 0.3	0.0 / 4.4
120-500	5.3 / 6.6	4.6 / 12.6	0.4 / 1.4	0.1 / 0.2	1.4 / 3.6
Total	905.9 / 1404.4	8.6 / 59.0	17.1 / 46.2	9.5 / 17.8	16.6 / 11.5
			27.1 / 77.0		

Table 5: Systematic uncertainties on the background estimate for $Z\gamma$ by the template method.

where N_{sig} is the number of observed signal events, A is the geometric and kinematic acceptance, ϵ is the selection efficiency for events in the acceptance, and \mathcal{L} is the integrated luminosity. The value of A is affected by the choice of PDF set and other theoretical uncertainties, while the value of ϵ is susceptible to errors from triggering and reconstruction. In order to control the efficiency uncertainties, we instead extract corrections to the efficiencies obtained from the simulation. These correction factors come from efficiency ratios $\rho_{\text{eff}} = \epsilon_{\text{data}}/\epsilon_{\text{MC}}$ derived by measuring the efficiency in the same way on data and simulation. We then replace the product $A_{\ell\nu\gamma(\ell\ell\gamma)} \times \epsilon$ by the product $\mathcal{F} \times \rho_{\text{eff}}$, where $\mathcal{F}_{\ell\nu\gamma(\ell\ell\gamma)} \equiv A_{\ell\nu\gamma(\ell\ell\gamma)} \times \epsilon_{\text{MC}}$ is the fraction of generated events selected in the simulation.

Eq. (4) can therefore be rewritten as:

$$\sigma = \frac{N_{\text{obs}} - N_{\text{bkg}}}{\mathcal{F} \cdot \rho_{\text{eff}} \cdot \mathcal{L}} \quad (5)$$

in which we also replaced the number of signal events N_{sig} by subtracting the estimated num-

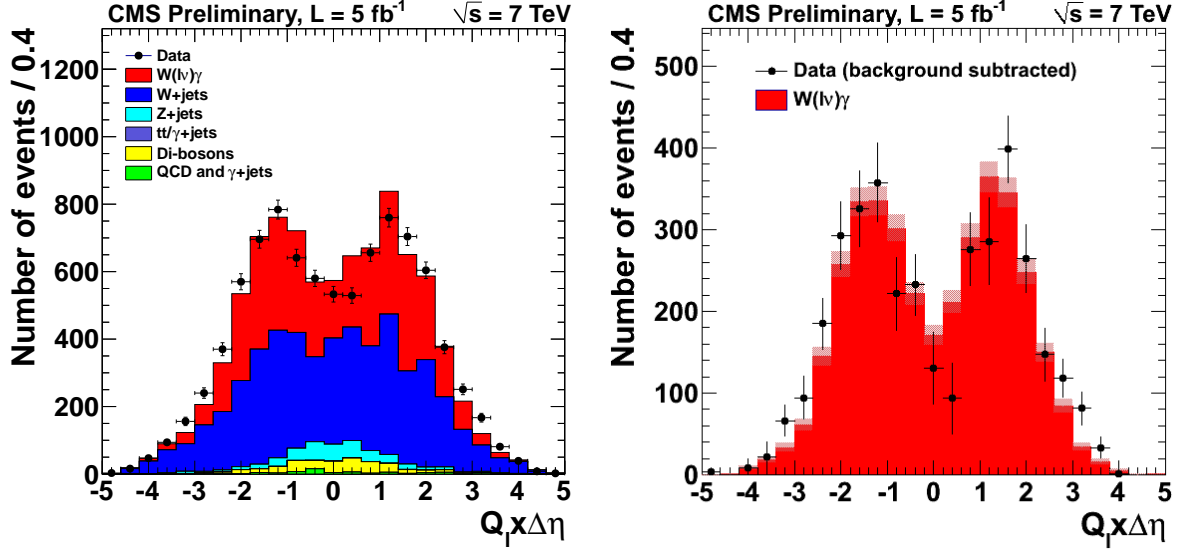


Figure 6: Event yields after event selection $Q_\ell \times \Delta\eta(\gamma, \ell)$, combined for $W\gamma \rightarrow \mu\nu\gamma$ and $W\gamma \rightarrow e\nu\gamma$. Yield from signal simulation is scaled to data signal yield. The right plot is background subtracted and errors include statistic and systematic errors.

Parameters	$Z\gamma \rightarrow ee\gamma$	$Z\gamma \rightarrow \mu\mu\gamma$
N_{obs}	4108 ± 64.1 (stat.)	6463 ± 80.4 (stat.)
$N_{\text{bkg}}^{\text{Data Driven}}$	905.9 ± 49.8 (stat.) ± 31.5 (syst.)	1404.3 ± 56.4 (stat.) ± 77.0 (syst.)
$N_{\text{bkg}}^{\text{other}}$	38.3 ± 2.8 (stat.)	23.7 ± 2.2 (stat.)
N_{sig}	3154.2 ± 81.0 (stat.) ± 95.1 (syst.)	5034.9 ± 98.2 (stat.) ± 213.2 (syst.)
$A \cdot \epsilon_{\text{MC}}$	0.132 ± 0.0018 (syst.)	0.196 ± 0.001 (stat.)
ρ_{eff}	0.929 ± 0.0466 (syst.)	0.945 ± 0.016 (syst.)
$\int \mathcal{L} dt$	5.0 ± 0.1 (syst.)	5.0 ± 0.1 (syst.)

Table 6: Summary of parameters for the $Z\gamma$ cross section measurement for full 2011 dataset.

ber of background events N_{bkg} from the observed number of selected events N_{obs} .

We calculate $\mathcal{F}_{\ell\nu\gamma(\ell\ell\gamma)}$ using MC simulation, as \mathcal{F} is defined as $N_{\text{accept}}/N_{\text{gen, kin}}$, where N_{accept} is the number of events passing all selection cuts, and $N_{\text{gen, kin}}$ is the number of generated events with $p_T^\gamma > 15$, $\Delta R_{\ell,\gamma} > 0.7$.

5.1 Systematic Uncertainties

Systematic uncertainties are grouped into five categories. The first group includes the uncertainties that affect the signal yield. These include uncertainties on lepton and photon energy scales. We vary the electron energy scale in data by 0.5% to estimate the contribution from inter-calibration of the ECAL detector. For photons the energy scale is varied by 1% in the ECAL barrel and 3% in the endcaps. To estimate the systematic effect on the measured cross section we re-evaluate N_{sig} for variations of each source of systematic uncertainty. In the case of the variation of the photon energy scale, the background subtraction is performed with signal and background templates that have been appropriately modified. This ensures that migrations of photons and misidentified photon-like jets across the low p_T^γ boundaries are properly accounted for when calculating this systematic uncertainty.

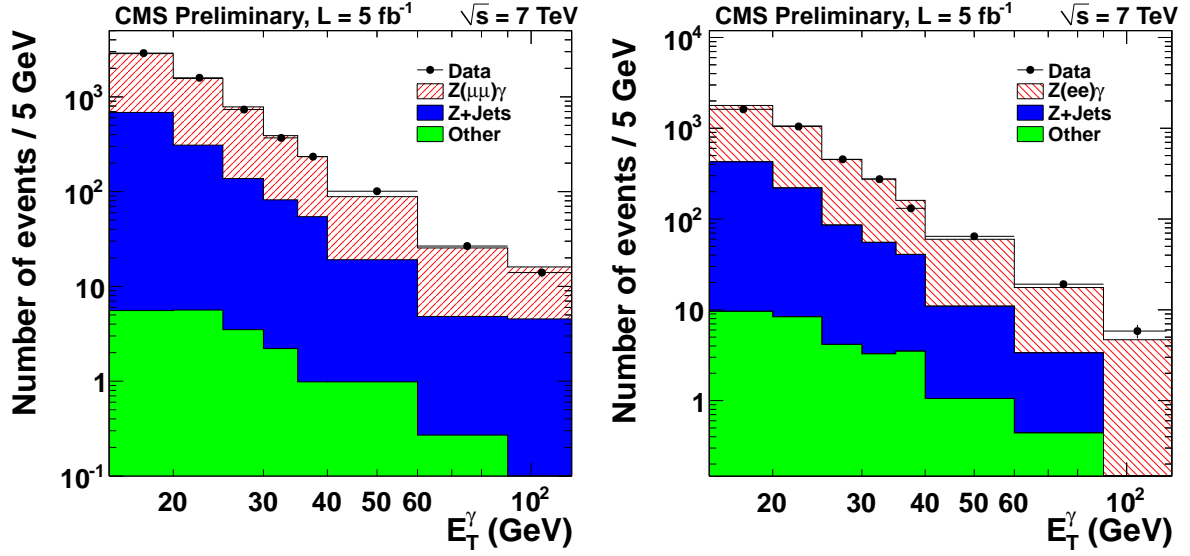


Figure 7: Photon candidate p_T spectrum (left) is given for data (black dots), signal MC simulation (red hatched histogram), and background from $Z/\gamma^*+\text{jets}$ (blue hatched histogram) for $Z\gamma \rightarrow \mu\mu\gamma$ (left) and $Z\gamma \rightarrow e\gamma$ (right).

In the second group, we combine the uncertainties that affect the product of the acceptance, reconstruction and identification efficiencies of final state objects, as determined from simulation. These include uncertainties on lepton and photon energy resolution, effects from pile-up (PU) interactions, and uncertainties in the PDF. The combined acceptance times efficiency, $A \cdot \epsilon$, is determined from MC simulation of the $V\gamma$ signal and is affected by the electron and photon energy resolution by way of migration of events in and out of acceptance. The electron energy resolution is determined in data using $Z \rightarrow ee$ events and calibrating to with respect to the known width of the Z boson peak following the same procedure employed in $H \rightarrow \gamma\gamma$ analysis [26]. To estimate the effect of the electron resolution on $A \cdot \epsilon$ each electron candidate's energy is randomly smeared by the energy resolution determined in data then standard selection is applied. The photon energy resolution is determined simultaneously with the photon energy scale in data following the description in Sec. A. The systematic effect of the photon resolution on $A \cdot \epsilon_{MC}$ is calculated by smearing, in a deterministic way, the reconstructed photon energy in simulation to match that in data.

The number of PU interactions per event is estimated from data using a convolution procedure that extracts the estimated PU from the per-bunch instantaneous luminosity recorded by the luminosity monitors. This methodology requires the total inelastic pp scattering cross section, 68 ± 3.4 mb, to estimate the number of PU events in a given bunch crossing. We estimate the systematic uncertainty due to modeling of the PU interactions by varying the total inelastic cross section within its uncertainties and estimate its effect on $A \cdot \epsilon_{MC}$. The uncertainties on parton distribution functions can alter the acceptance in simulation, especially for very forward, low x , $V\gamma$ events. To estimate the systematic effect on $A \cdot \epsilon_{MC}$, LHAPDF [27] was used to generate per-event weights using variations along the 21 sets of eigenvectors of the CTEQ6L PDF set [28]. To assign an uncertainty due to variation of the PDF on the acceptance we use the “modified tolerance method” as recommended by the PDF4LHC interim report [29]. The uncertainty on signal modeling is taken from the acceptance difference between MCFM and MADGRAPH.

The third group includes the systematic uncertainties affecting the data vs. simulation correction factors ρ_{eff} for the efficiencies of the trigger, reconstruction, and identification requirements. These include lepton trigger, lepton and photon reconstruction and identification, and E_T selection efficiencies for the $W\gamma$ process. The lepton efficiencies are determined by the “tag-and-probe” method in the same way for data and simulation, and the uncertainties are taken by varying the background modeling, and fit range in “tag-and-probe” method. An additional uncertainty is added by taking into account the difference between the measured and true efficiency in Monte Carlo simulation sample.

The fourth category comprises uncertainties on the background yield. These are dominated by the uncertainties on the estimations of W +jets and Z +jets background from data. The comparison of the $\sigma_{i\eta j\eta}$ distributions for the probe in data and simulation indicates that the mean of the $\sigma_{i\eta j\eta}$ distribution in data is smaller than that in simulation by 0.9×10^{-4} (2.0×10^{-4}) for barrel(endcap) and corresponds to 1% (0.8%) of the average of the simulated photon $\sigma_{i\eta j\eta}$ values, which are corrected for the observed shift. The signal $\sigma_{i\eta j\eta}$ template in simulation needs to be corrected by 0.9×10^{-4} for barrel and 2.1×10^{-4} for endcap to match $\sigma_{i\eta j\eta}$ templates observed in data. We take this difference as a systematic uncertainty on signal template and re-calculate the background estimation to measure its effect on the final result.

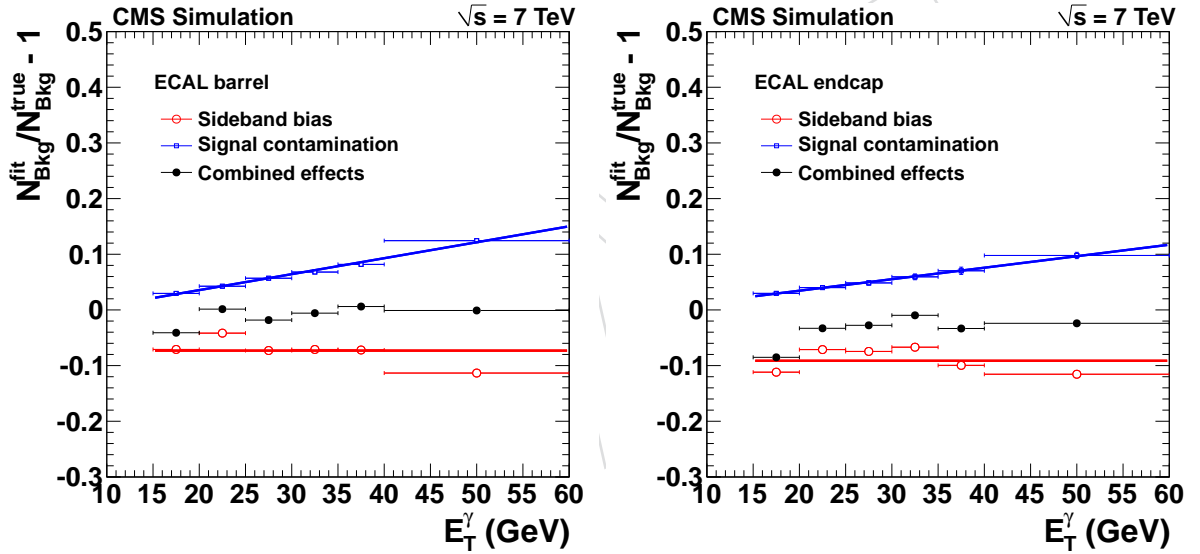


Figure 8: The uncertainty on background template for barrel (left) and endcap (right). The change in the estimated number of background events due to “anti-isolation” requirement (sideband bias) is given as a function of E_T^γ as red circles, while the contamination from genuine photons are given as blue dots. The overall effect is given as red dots.

To obtain the background $\sigma_{i\eta j\eta}$ template we use photon-like jets selected by requiring tracker “anti-isolation” requirement. Using this template to infer the background from photon-like jets that pass the full photon isolation requirements can cause a bias if the $\sigma_{i\eta j\eta}$ template is correlated with tracker isolation. A contribution from genuine photons that pass “anti-isolation” requirement can also cause the bias in estimation of the background. We estimate the effects from these sources in simulation where one can distinguish genuine photons from jets and found the effect the overall effect to be small (see Fig. 8).

Since smoothing is used to determine a continuous function that describes the $\sigma_{i\eta j\eta}$ distribution of the background, the effect of the statistical sampling of the background probability density

function true underlying shape must be understood. To study this, a bootstrapping technique exploiting simulation is used to generate a known true distribution of background from which we can throw toy template distributions. These toy distributions are then smoothed themselves and used to fit the background fraction in data. The results of each toy template distribution and fit is saved and the variance associated with the statistical fluctuation in the template is recorded and taken as a systematic error.

The uncertainties on the smaller background contributions are taken from the statistical uncertainty of the simulation samples.

Finally, an additional uncertainty due to the measurement of the integrated luminosity is considered. This uncertainty is 2.2% [30].

5.2 Results for the $W\gamma$ cross section

A summary of all of the systematic uncertainties on $W\gamma$ cross section measurement is given in Table 7 for both the electron and muon channels. The main source of uncertainty in both cases, apart from the uncertainty on luminosity, is due to the estimation of background from data using the template method. More detailed information can be found in Section 5.1.

Source	Systematic uncertainty	$ev\gamma$	$\mu\nu\gamma$
		Effect on N_{sig}	
Electron and photon energy scale	ele: 0.5%; pho: 1% (EB), 3% (EE)	2.9%	n/a
Photon energy scale	1% (EB), 3% (EE)	n/a	2.9%
Muon p_T scale	0.2%	n/a	0.6%
Total uncertainty on N_{sig}		2.9%	3.0%
Source	Systematic uncertainty	Effect on $\mathcal{F} = A \cdot \epsilon_{\text{MC}}$	
Electron and photon energy resolution	1% (EB), 3% (EE)	0.3%	n/a
Photon energy resolution	1% (EB), 3% (EE)	n/a	0.1%
Muon p_T resolution	0.6%	n/a	0.1%
Pileup	Shift data PU distribution by $\pm 5\%$	2.4%	0.8%
PDF	CTEQ6L re-weighting	0.9%	0.9%
Signal modeling	5%	5.0%	5.0%
Total uncertainty on $\mathcal{F} = A \cdot \epsilon_{\text{MC}}$		5.6%	5.1%
Source	Systematic uncertainty	Effect on ρ_{eff}	
Lepton reconstruction		0.4%	1.5%
Lepton trigger		0.1%	0.9%
Lepton ID and isolation		2.5%	0.9%
\cancel{E}_T selection		1.4%	1.5%
Photon ID and isolation	0.5% (EB), 1.0% (EE)	0.5%	0.5%
Total uncertainty on ρ_{eff}		2.9%	2.5%
Source	Systematic uncertainty	Effect on background yield	
Template method		9.3%	9.0%
Electron misidentification		7.1%	5.2%
MC prediction		6.2%	6.8%
Total uncertainty on background		7.1%	8.3%
Source	Systematic uncertainty	Effect on luminosity	
Luminosity	2.2%	2.2%	2.2%

Table 7: Summary of systematic uncertainties for the $W\gamma$ cross section measurement.

The estimated cross sections are:

$$\sigma(pp \rightarrow W\gamma \rightarrow ev\gamma) = 36.6 \pm 1.2 \text{ (stat.)} \pm 4.3 \text{ (syst.)} \pm 0.8 \text{ (lumi.) pb.}$$

$$\sigma(pp \rightarrow W\gamma \rightarrow \mu\nu\gamma) = 37.5 \pm 0.9 \text{ (stat.)} \pm 4.4 \text{ (syst.)} \pm 0.8 \text{ (lumi.) pb.}$$

The combination of the cross sections, performed using a Best Linear Unbiased Estimator (BLUE) [31], is:

$$\sigma(pp \rightarrow W\gamma \rightarrow \ell\nu\gamma) = 37.0 \pm 0.8 \text{ (stat.)} \pm 4.0 \text{ (syst.)} \pm 0.8 \text{ (lumi.) pb.}$$

All three results are consistent with the theoretical NLO cross section 31.81 ± 1.8 pb., computed with MCFM, within uncertainties.

5.3 Results for the $Z\gamma$ Cross Section

The systematic uncertainties are listed in Table 8. The measured cross sections are:

$$\sigma(pp \rightarrow Z\gamma \rightarrow ee\gamma) = 5.20 \pm 0.13 \text{ (stat.)} \pm 0.30 \text{ (syst.)} \pm 0.11 \text{ (lumi.) pb.}$$

$$\sigma(pp \rightarrow Z\gamma \rightarrow \mu\mu\gamma) = 5.43 \pm 0.10 \text{ (stat.)} \pm 0.29 \text{ (syst.)} \pm 0.12 \text{ (lumi.) pb.}$$

The combination of the cross sections, performed with the BLUE method [31] is:

$$\sigma(pp \rightarrow Z\gamma \rightarrow \ell\ell\gamma) = 5.33 \pm 0.08 \text{ (stat.)} \pm 0.25 \text{ (syst.)} \pm 0.12 \text{ (lumi.) pb.}$$

All three results are consistent with the theoretical NLO cross section 5.45 ± 0.27 pb., computed with MCFM, within uncertainties.

Source	Systematic uncertainty	$ee\gamma$	$\mu\mu\gamma$
		Effect on N_{sig}	
Electron and photon energy scale	ele: 0.5%; pho: 1% (EB) 3% (EE)	3.0 %	n/a
Photon energy scale	1% (EB) 3% (EE)	n/a	4.19%
Muon p_T scale	0.2%	n/a	0.60%
Total uncertainty on N_{sig}		3.0 %	4.23%
Source	Systematic uncertainty	Effect on $\mathcal{F} = A \cdot \epsilon_{\text{MC}}$	
Electron and photon energy resolution	1% (EB), 3% (EE)	0.2 %	n/a
Photon energy resolution	1% (EB), 3% (EE)	n/a	0.06%
Muon p_T resolution	0.6%	n/a	0.08%
Pileup	Shift data PU distribution by $\pm 5\%$	0.6 %	0.44%
PDF	CTEQ6L re-weighting	1.1%	1.10%
Signal Modeling		0.6 %	1.10%
Total uncertainty on $\mathcal{F} = A \cdot \epsilon_{\text{MC}}$		1.4 %	1.22%
Source	Systematic uncertainty	Effect on ρ_{eff}	
Lepton reconstruction		0.8 %	1.0 %
Lepton trigger		0.1 %	1.0 %
Lepton ID and isolation		5.0 %	2.3 %
Photon ID and isolation	0.5% (EB), 1.0% (EE)	0.5 %	1.00%
Total uncertainty on ρ_{eff}		5.1 %	2.51%
Source	Systematic uncertainty	Effect on background yield	
Template method		4.4%	5.5%
Total uncertainty on background		4.4 %	5.5%
Source	Systematic uncertainty	Effect on luminosity	
Luminosity	2.2%	2.2%	2.2%

Table 8: Summary of systematic uncertainties for the $Z\gamma$ cross section measurement for full 2011 dataset.

5.4 Comparisons to MCFM Predictions

Finally, we present a summary of the $W\gamma$ and $Z\gamma$ cross sections measured with different lower bounds on the photon p_T . We find no significant disagreement with the MCFM prediction for $W\gamma$ after accounting for all systematic uncertainties when requiring the photon p_T to be larger than 60 and 90 GeV.

The measured cross sections, predictions, and their errors are summarized in Table 9 and in Fig. 9.

$W\gamma$		
	Electron Channel (pb)	Muon Channel (pb)
$p_T^\gamma > 60$ GeV	$0.77 \pm 0.07(\text{stat.}) \pm 0.13(\text{syst.}) \pm 0.02(\text{lumi.})$	$0.76 \pm 0.06(\text{stat.}) \pm 0.08(\text{syst.}) \pm 0.02(\text{lumi.})$
Combination	$0.76 \pm 0.05(\text{stat.}) \pm 0.08(\text{syst.}) \pm 0.02(\text{lumi.})$ pb	
Prediction	0.58 ± 0.08 (pb)	
$p_T^\gamma > 90$ GeV	$0.173 \pm 0.034(\text{stat.}) \pm 0.037(\text{syst.}) \pm 0.004(\text{lumi.})$	$0.248 \pm 0.035(\text{stat.}) \pm 0.048(\text{syst.}) \pm 0.005(\text{lumi.})$
Combination	$0.200 \pm 0.025(\text{stat.}) \pm 0.038(\text{syst.}) \pm 0.004(\text{lumi.})$ pb	
Prediction	0.173 ± 0.026 pb	
$Z\gamma$		
$p_T^\gamma > 60$ GeV	$0.142 \pm 0.019(\text{stat.}) \pm 0.019(\text{syst.}) \pm 0.003(\text{lumi.})$	$0.139 \pm 0.013(\text{stat.}) \pm 0.015(\text{syst.}) \pm 0.003(\text{lumi.})$
Combination	$0.140 \pm 0.011(\text{stat.}) \pm 0.013(\text{syst.}) \pm 0.003(\text{lumi.})$ pb	
Prediction	0.124 ± 0.009 pb	
$p_T^\gamma > 90$ GeV	$0.047 \pm 0.013(\text{stat.}) \pm 0.010(\text{syst.}) \pm 0.001(\text{lumi.})$	$0.046 \pm 0.008(\text{stat.}) \pm 0.010(\text{syst.}) \pm 0.001(\text{lumi.})$
Combination	$0.046 \pm 0.007(\text{stat.}) \pm 0.009(\text{syst.}) \pm 0.001(\text{lumi.})$ pb	
Prediction	0.040 ± 0.004 pb	

Table 9: The summary of the cross section measurements and predictions for $p_T^\gamma > 60$ and 90 GeV for $W\gamma$ and $Z\gamma$.

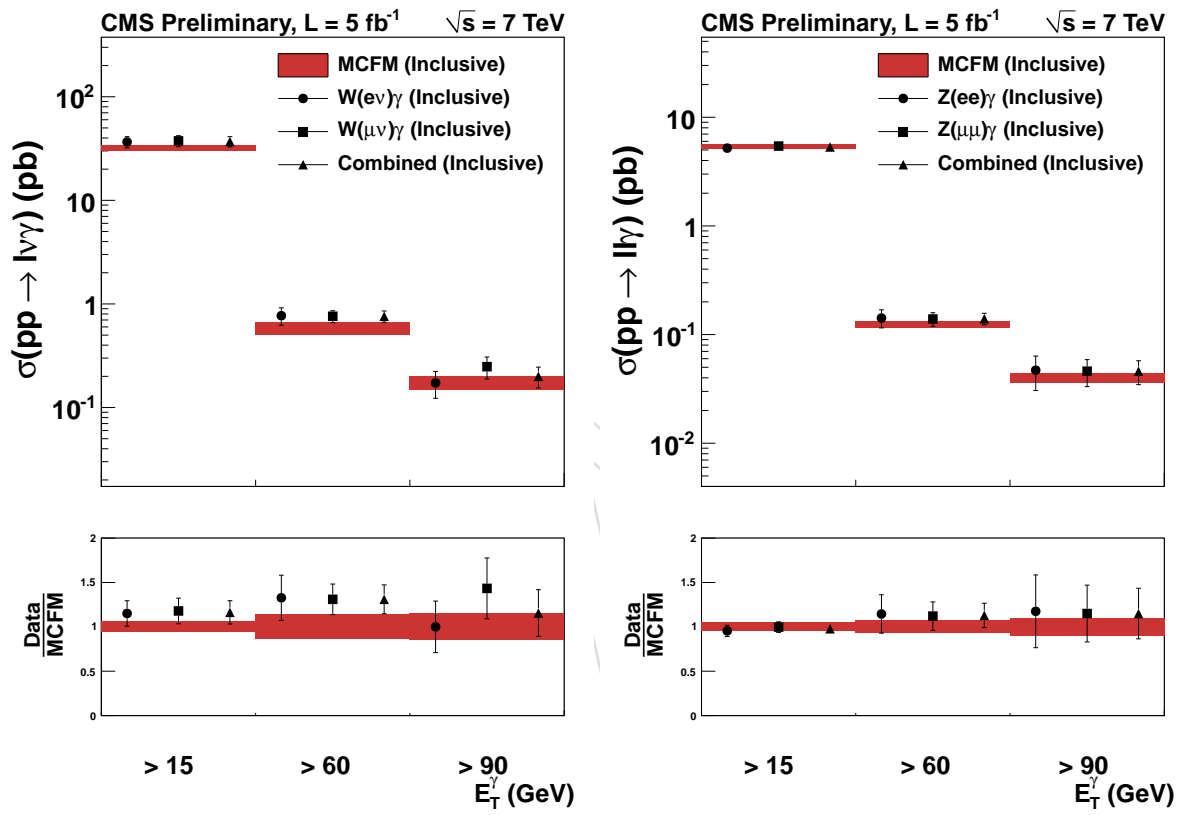


Figure 9: The left plot shows the summary of all cross section measurements and comparisons to theory for the $W\gamma$ measurement, the right plot is for $Z\gamma$.

6 Anomalous Triple Gauge Couplings in $W\gamma$ and $Z\gamma$ Processes

To extract limits on anomalous triple gauge couplings we use a counting experiment based on bins in p_T^γ . 95% upper limits on the aTGC values are set using the modified frequentist CLs technique [32].

6.1 $WW\gamma$ coupling

The most general Lorentz invariant effective Lagrangian that describes $WW\gamma$ and WWZ couplings has 14 independent parameters [33, 34], seven for each vertex. Assuming C and P conservation, only six independent couplings remain that describe the $WW\gamma$ and WWZ vertices with an effective Lagrangian normalized by the electroweak coupling given below:

$$\frac{\mathcal{L}_{WWV}}{g_{WWV}} = i g_1^V (W_{\mu\nu}^\dagger W^\mu V^\nu - W_\mu^\dagger V_\nu W^{\mu\nu}) + i \kappa_V W_\mu^\dagger W_\nu V^{\mu\nu} + \frac{i \lambda_V}{M_W^2} W_{\delta\mu}^\dagger W_\nu^\mu V^{\nu\delta}, \quad (6)$$

where $V = \gamma$ or Z , W^μ are the W^\pm fields, $W_{\mu\nu} = \partial_\mu W_\nu - \partial_\nu W_\mu$, and overall couplings $g_{WW\gamma} = -e$ and $g_{WWZ} = -e \cot \theta_W$, where θ_W is the Weinberg angle. Assuming electromagnetic gauge invariance, $g_1^\gamma = 1$, the remaining parameters that describe $WW\gamma$ and WWZ couplings are g_1^Z , κ_Z , κ_γ , λ_Z , and λ_γ . In the SM, $\lambda_Z = \lambda_\gamma = 0$ and $g_1^Z = \kappa_Z = \kappa_\gamma = 1$. In this analysis, we follow the convention to describe the couplings in terms of their deviation from the SM values: $\Delta g_1^Z \equiv g_1^Z - 1$, $\Delta \kappa_Z \equiv \kappa_Z - 1$, and $\Delta \kappa_\gamma \equiv \kappa_\gamma - 1$.

These five couplings are further reduced to three independent couplings if one requires the Lagrangian to be $SU(2)_L \times U(1)_Y$ invariant:

$$\Delta \kappa_Z = \Delta g_1^Z - \Delta \kappa_\gamma \cdot \tan^2 \theta_W, \quad \lambda = \lambda_\gamma = \lambda_Z. \quad (7)$$

In this study we measure $\Delta \kappa_\gamma$ and λ_γ from $W\gamma$ production.

6.2 $ZZ\gamma$ and $Z\gamma\gamma$ couplings

The most general vertex function [35] for $ZZ\gamma$ can be written as

$$\begin{aligned} \Gamma_{ZZ\gamma}^{\alpha\beta\mu}(q_1, q_2, P) = \frac{P^2 - q_1^2}{m_Z^2} & \left[h_1^Z (q_2^\mu g^{\alpha\beta} - q_2^\alpha g^{\mu\beta}) \right. \\ & + \frac{h_2^Z}{m_Z^2} P^\alpha [(P \cdot q_2) g^{\mu\beta} - g_2^\mu P^\beta] \\ & + h_3^Z \epsilon^{\mu\alpha\beta\rho} q_{2\rho} \\ & \left. + \frac{h_4^Z}{m_Z^2} P^\alpha \epsilon^{\mu\beta\rho\sigma} P_\rho q_{2\sigma} \right] \end{aligned} \quad (8)$$

with the $Z\gamma\gamma$ vertex obtained by the following replacements:

$$\frac{P^2 - q_1^2}{m_Z^2} \rightarrow \frac{P^2}{m_Z^2} \quad \text{and} \quad h_i^Z \rightarrow h_i^\gamma, \quad i = 1, \dots, 4. \quad (9)$$

The couplings h_i^V with $V = Z, \gamma$ and $i = 1, 2$ violate CP symmetry, while those with $i = 3, 4$ are CP -even. Although at tree level all these couplings in the SM are equal to zero, at one-loop level the CP -conserving couplings are $\mathcal{O}(10^{-4})$. As the sensitivity to both CP -odd and CP -even couplings using p_T^γ are the same, we interpret the results in terms of h_i^V with $i = 3, 4$.

6.3 Search for Anomalous Couplings in $W\gamma$ and $Z\gamma$ Production

We generate the expected aTGC signal using SHERPA generator [18] for the detector simulation of the $W\gamma+n$ jet and $Z\gamma+n$ jet ($n \leq 1$) processes.

For $W\gamma$ two aTGC parameters, $\Delta\kappa_\gamma$ and λ_γ , are freely varied while g_1^Z is set to the SM value, using the ‘equal couplings’ scenario of the LEP parameterization [36]. For $Z\gamma$, limits are set on the anomalous couplings h_3^V and h_4^V with $V = Z, \gamma$ with two couplings being varied at a time. When limits are set on the Z-type couplings, the γ couplings are set to their standard model values.

We set one and two dimensional limits on the aTGC parameters $\Delta\kappa_\gamma$ and λ_γ for $W\gamma$ and h_3^V and h_4^V for $Z\gamma$. In the case of setting one dimensional limits the parameters whose limits are not being estimated are set to their standard model values. The 95% C.L. two-dimensional contours are given in Fig. 10 for $W\gamma$ and Fig. 11 for $Z\gamma$. Corresponding one-dimensional limits are listed in Table 10 for $W\gamma$ and Table 11 for $Z\gamma$.

	$\Delta\kappa_\gamma$	λ_γ
$W\gamma \rightarrow e\nu\gamma$	[-0.45, 0.36]	[-0.059, 0.046]
$W\gamma \rightarrow \mu\nu\gamma$	[-0.46, 0.34]	[-0.057, 0.045]
$W\gamma \rightarrow \ell\nu\gamma$	[-0.38, 0.29]	[-0.050, 0.037]

Table 10: One dimensional limits on aTGCs at 95% C.L. for $W\gamma$, no form factor is used.

	h_3^γ	h_4^γ	h_3^Z	h_4^Z
$Z\gamma \rightarrow ee\gamma$	[-0.013, 0.013]	$[-1.1, 1.1] \times 10^{-4}$	[-0.011, 0.011]	$[-9.9, 9.5] \times 10^{-5}$
$Z\gamma \rightarrow \mu\mu\gamma$	[-0.013, 0.013]	$[-1.1, 1.2] \times 10^{-4}$	[-0.011, 0.011]	$[-1.0, 1.1] \times 10^{-4}$
$Z\gamma \rightarrow \ell\ell\gamma$	[-0.010, 0.010]	$[-8.8, 8.8] \times 10^{-5}$	$[-8.6, 8.4] \times 10^{-3}$	$[-8.0, 7.9] \times 10^{-5}$

Table 11: One-dimensional limits on $Z\gamma$ anomalous trilinear gauge couplings.

7 Summary

We presented an updated measurement of the $V\gamma + X$ production cross sections using leptonic decays of $W \rightarrow e\nu$, $W \rightarrow \mu\nu$, $Z \rightarrow ee$, and $Z \rightarrow \mu\mu$. The measurements are based on the full 7 TeV dataset recorded by the CMS experiment at the LHC in 2011 and corresponds to an integrated luminosity of 5 fb^{-1} . The measured cross sections $\sigma(pp \rightarrow W\gamma) = 37.0 \pm 0.8 \text{ (stat.)} \pm 4.0 \text{ (syst.)} \pm 0.8 \text{ (lumi.) pb}$ and $\sigma(pp \rightarrow Z\gamma) = 5.33 \pm 0.08 \text{ (stat.)} \pm 0.25 \text{ (syst.)} \pm 0.12 \text{ (lumi.) pb}$ with $p_T^\gamma > 15 \text{ GeV}$ are found to be consistent with the standard model prediction. The agreements still hold with higher p_T^γ thresholds of 60 and 90 GeV. The most stringent limits on anomalous trilinear $WW\gamma$, $ZZ\gamma$, and $Z\gamma\gamma$ gauge couplings are set at 95% confidence level. No evidence for physics beyond the SM is observed.

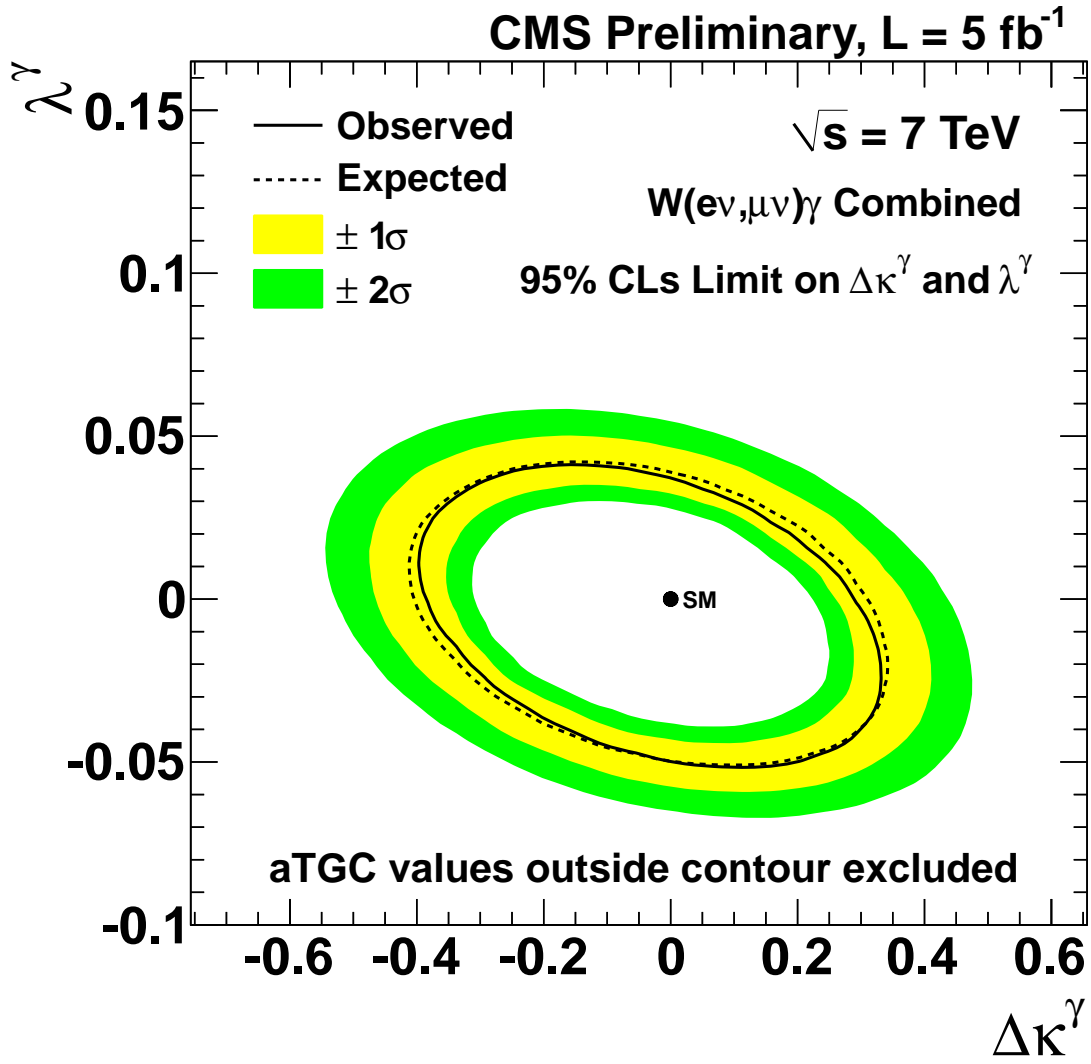


Figure 10: 95% confidence level for the combination of electron and muon channels contour for $WW\gamma$ coupling.

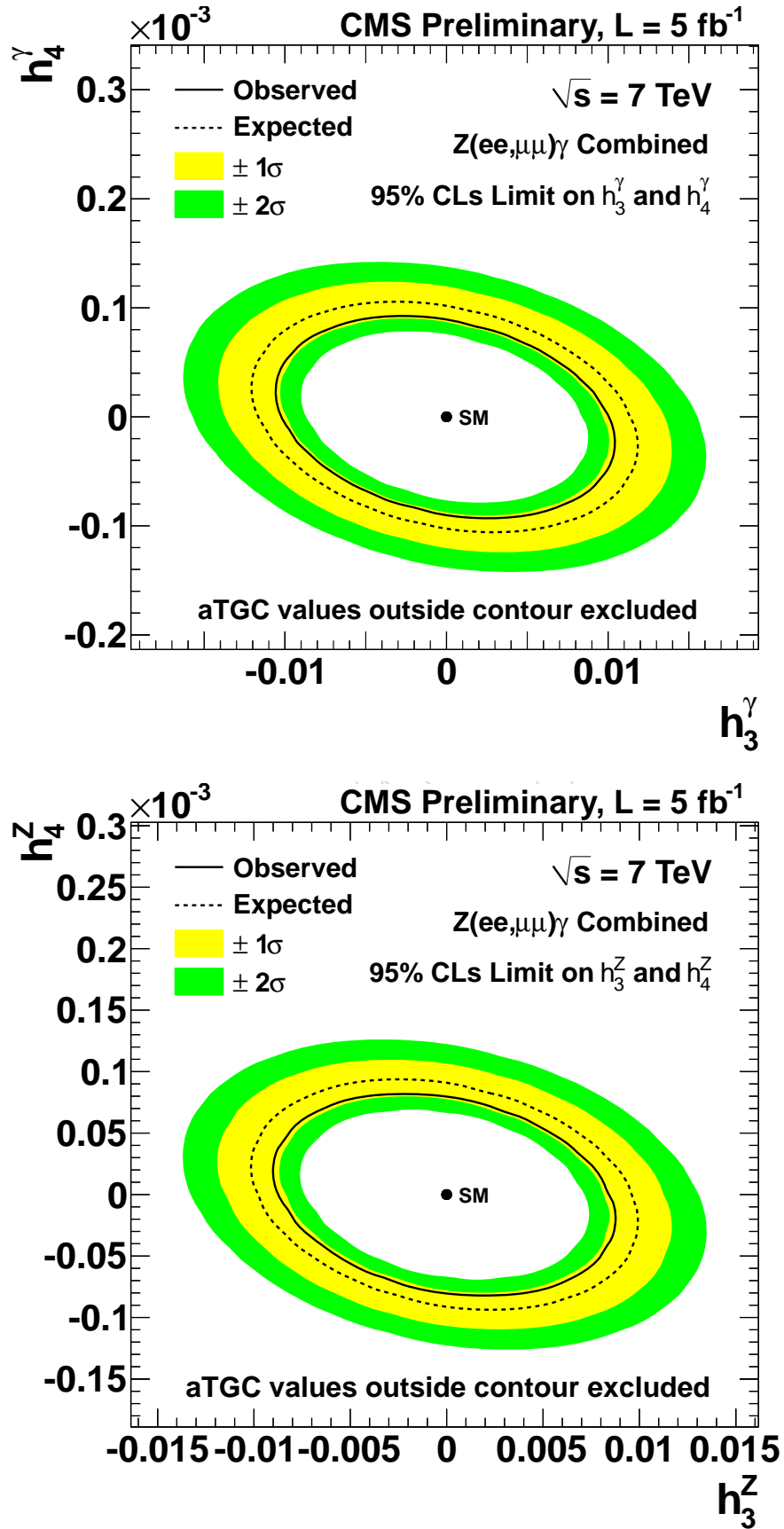


Figure 11: 95% confidence level contours for $Z\gamma\gamma$ (left) and $ZZ\gamma$ (right) couplings from the combined information of the electron and muon channels.

References

- [1] LEP Electroweak Working Group Collaboration, “A combination of preliminary electroweak measurements and constraints on the standard model”, (2004).
arXiv:0412015v2.
- [2] L3 Collaboration, “Measurement of energetic single photon production at LEP”, *Phys. Lett. B* **346** (1995) 190, doi:10.1016/0370-2693(95)00023-E.
- [3] L3 Collaboration, “Study of the $e^+e^- \rightarrow Z\gamma$ process at LEP and limits on triple neutral-gauge-boson couplings”, *Phys. Lett. B* **597** (2004) 119,
doi:10.1016/j.physletb.2004.07.002.
- [4] OPAL Collaboration, “Study of Z pair production and anomalous couplings in e^+e^- collisions at \sqrt{s} between 190 GeV and 209 GeV”, *Eur. Phys. J. C* **32** (2003) 303,
doi:10.1140/epjc/s2003-01467-x.
- [5] D0 Collaboration, “Measurement of $p\bar{p} \rightarrow W\gamma + X$ cross section at $\sqrt{s} = 1.96$ TeV and $WW\gamma$ anomalous coupling limits”, *Phys. Rev. D* **71** (2005) 091108,
doi:10.1103/PhysRevD.71.091108.
- [6] D0 Collaboration, “First study of radiation-amplitude zero in $W\gamma$ production and limits on anomalous $WW\gamma$ couplings at $\sqrt{s} = 1.96$ TeV”, *Phys. Rev. Lett.* **100** (2008) 241805,
doi:10.1103/PhysRevLett.100.241805.
- [7] D0 Collaboration, “Combined measurements of anomalous charged trilinear gauge-boson couplings from diboson production in p-pbar collisions at $\sqrt{s} = 1.96$ TeV”, (2009). arXiv:0907.4952v2.
- [8] CDF Collaboration, “Measurement of $Z\gamma$ production in $p\bar{p}$ collisions at $\sqrt{s} = 1.96$ TeV”, *Phys. Rev. D* **82** (2010) 031103, doi:10.1103/PhysRevD.82.031103.
- [9] D0 Collaboration, “ $Z\gamma$ production and limits on anomalous $ZZ\gamma$ and $Z\gamma\gamma$ couplings in $p\bar{p}$ collisions at $\sqrt{s} = 1.96$ TeV”, *Phys. Lett. B* **653** (2007) 378,
doi:doi:10.1016/j.physletb.2007.08.035.
- [10] D0 Collaboration, “Measurement of the $Z\gamma \rightarrow \nu\nu\gamma$ cross section and limits on anomalous $ZZ\gamma$ and $Z\gamma\gamma$ couplings in $p\bar{p}$ collisions at $\sqrt{s} = 1.96$ TeV”, *Phys. Rev. Lett.* **102** (2009) 201802, doi:10.1103/PhysRevLett.102.201802.
- [11] CMS Collaboration, “Measurement of W^+W^- production and search for the Higgs boson in pp collisions at $\sqrt{s} = 7$ TeV”, *Phys. Lett. B* **699** (2011) 25.
- [12] CMS Collaboration, “Measurement of $W\gamma$ and $Z\gamma$ production in pp collisions at $\sqrt{s} = 7$ TeV”, *Phys. Lett. B* **701** (2011) 535.
- [13] ATLAS Collaboration, “Measurement of $W\gamma$ and $Z\gamma$ production cross sections in pp collisions at $\sqrt{s} = 7$ TeV and limits on anomalous triple couplings with the ATLAS detector”, *Phys. Lett. B* **701** (2012) 535, arXiv:hep-ex/1205.2531.
- [14] J.M. Campbell, R.K. Ellis, and C. Williams, “Vector boson pair production at the LHC”,
arXiv:1105.0020.
- [15] CMS Collaboration, “The CMS experiment at the CERN LHC”, *JINST* **3** (2008) S08004,
doi:10.1088/1748-0221/3/08/S08004.

- [16] J. Alwal *et al.*, “MADGRAPH/MADEVENT v4: The New Web Generation”, *JHEP* **09** (2007) 028, doi:10.1088/1126-6708/2007/09/028.
- [17] T. Sjöstrand, S. Mrenna, and P. Skands, “PYTHIA 6.4 physics and manual”, *JHEP* **05** (2006) 026, doi:10.1088/1126-6708/2006/05/026.
- [18] T. Gleisberg *et al.*, “Event generation with SHERPA 1.1”, *JHEP* **02** (2009) 007, doi:10.1088/1126-6708/2009/02/007.
- [19] J. Pumplin, D. R. Stump, J. Huston, H. L. Lai, P. Nadolsky and W. K. Tung, “New generation of parton distributions with uncertainties from global QCD analysis”, *JHEP* **0207** (2002) 012.
- [20] GEANT4 Collaboration, “GEANT4: A simulation toolkit”, *Nucl. Instrum. Meth.* **A506** (2003) 250, doi:10.1016/S0168-9002(03)01368-8.
- [21] CMS Collaboration, “Performance of CMS muon reconstruction in pp collision events at $\sqrt{s} = 7$ TeV”, arXiv:1206.4071.
- [22] CMS Collaboration Collaboration, “Measurement of the Differential Cross Section for Isolated Prompt Photon Production in pp Collisions at 7 TeV”, *Phys.Rev.* **D84** (2011) 052011, doi:10.1103/PhysRevD.84.052011, arXiv:1108.2044.
- [23] M. Cacciari, “FastJet: A Code for fast k_t clustering, and more”, arXiv:hep-ph/0607071.
- [24] CMS Collaboration, “Particle-flow commissioning with muons and electrons from J/Psi, and W events at 7 TeV”, *CMS PAS* **PFT-2010-003** (2010).
- [25] K. S. Cranmer, “Kernel estimation in high-energy physics”, *Comput. Phys. Commun.* **136** (2001) 198–207, doi:10.1016/S0010-4655(00)00243-5, arXiv:hep-ex/0011057.
- [26] CMS Collaboration, “Search for the standard model Higgs boson decaying into two photons in pp collisions at $\sqrt{s} = 7$ TeV”, *Phys. Lett. B* **710** (2012) 403–425.
- [27] D. Bourilkov, R. C. Group, and M. R. Whalley, “LHAPDF: PDF use from the Tevatron to the LHC”, arXiv:hep-ph/0605240.
- [28] J. Pumplin, D. Stump, J. Huston et al., “New generation of parton distributions with uncertainties from global QCD analysis”, *JHEP* **0207** (2002) 012, arXiv:hep-ph/0201195.
- [29] M. Botje, J. Butterworth, A. Cooper-Sarkar et al., “The PDF4LHC Working Group Interim Recommendations”, arXiv:1101.0538.
- [30] T. C. Collaboration, “Absolute Calibration of the Luminosity Measurement at CMS : Winter 2012 Update”,.
- [31] L. Lyons, G. Gibaut, and P. Clifford, “How to combine correlated estimates of a single physical quantity”, *Nucl. Instrum. Meth.* **A270** (1988) 110, doi:10.1016/0168-9002(88)90018-6.
- [32] G. Cowan, K. Cranmer, E. Gross, O. Vitells, “Asymptotic formulae for likelihood-based tests of new physics”, *Eur.Phys.J.* **C71** (2011) 1554, doi:10.1140/epjc/s10052-011-1554-0.

- [33] K. Hagiwara, R.D. Peccei, and D. Zeppenfeld, "Probing the Weak Boson Sector in $e^+e^- \rightarrow W^+W^-$ ", *Nucl. Phys.* **B282** (1987) 253, doi:doi:10.1016/0550-3213(87)90685-7.
- [34] K. Hagiwara, J. Woodside, and D. Zeppenfeld, "Measuring The WWZ Coupling At The Tevatron", *Phys. Rev.* **D41** (1990) 2113, doi:10.1103/PhysRevD.41.2113.
- [35] U. Baur and E. Berger, "Probing the weak-boson sector in $Z\gamma$ production at hadron colliders", *Phys. Rev.* **D47** (1993) 4889, doi:10.1103/PhysRevD.47.4889.
- [36] G. Gounaris, J. Kneur, D. Zeppenfeld et al., "Triple gauge boson couplings", arXiv:hep-ph/9601233.
- [37] S. Gadatsch and M. Baak, "Template morphing in many dimensions, with several fit parameters", *Talk Given December 2, 2009 INDICO* (2009).

A Photon Energy Scale and Resolution

The width and peak position of the Z boson can be exploited to measure photon energy resolution and determine the absolute photon energy scale using the data itself. The $Z \rightarrow \mu\mu\gamma$ process is the only source of pure energetic photons in the hadron collider environment. Requiring the $\mu\mu\gamma$ invariant mass to be within 30 GeV of the Z boson pole mass reduces the Z+jets background to a negligible level.

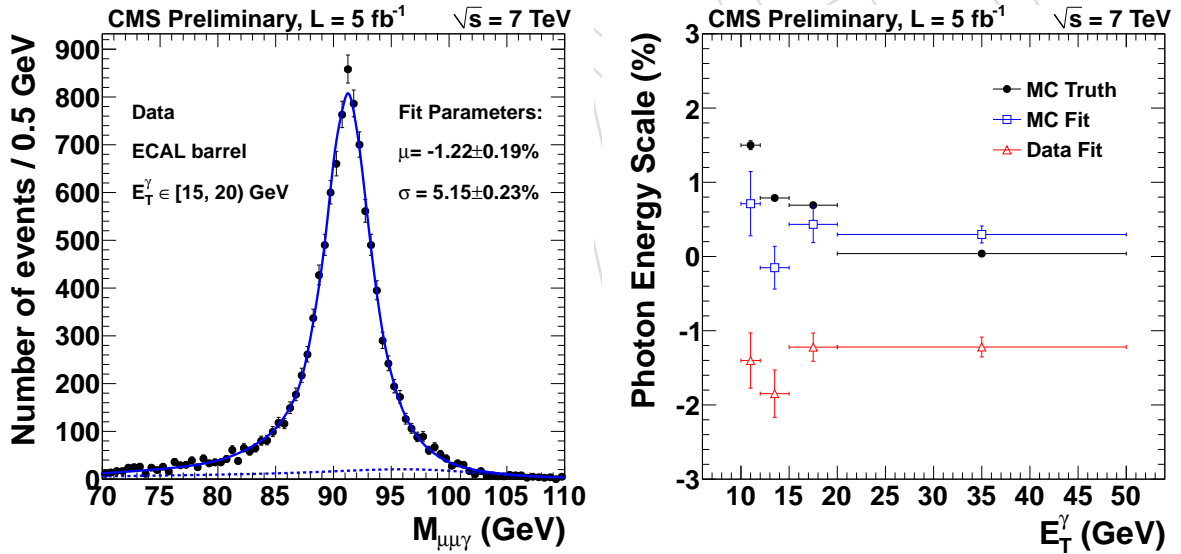


Figure 12: Left: The invariant mass of the $\mu\mu\gamma$ system for $Z \rightarrow \mu\mu\gamma$ data events fit to a model. The photon is required to be in the barrel and have transverse energy between 15 and 20 GeV. The photon energy scale and resolution and the fraction of the signal events are floated in the fit. Right: The photon energy scale as a function of the photon transverse energy for the simulation (MC Truth) and for a fit to the simulation (MC Fit) and to the data (Data Fit).

We define the scale s as the mode of the distribution of the photon energy response $x = E^\gamma / E_{\text{true}}^\gamma - 1$ where E^γ and E_{true}^γ are the reconstructed and true photon energies. The photon energy resolution r is defined as half of the shortest interval containing 68.3% of the photon energy response distribution.

To estimate the true scale and resolution in the simulation, we use directly the set of the energy responses in $Z \rightarrow \mu\mu\gamma$ sample. We smooth the distribution using a kernel density estimator [25] to obtain a non-parametric description of the input photon energy response density $f_0(x)$ with scale s_0 and resolution r_0 .

We then introduce the dependence on the scale s and resolution r by a linear transformation of the response:

$$\begin{aligned} x &\rightarrow x' = a(s, r) + b(s, r) x = x_0(x, s, r), \\ f_0(x) &\rightarrow f(x|s, r) = f_0(x_0(x, s, r)), \end{aligned} \quad (10)$$

where the scale and resolution dependent photon energy response $x' = x_0(x, s, r)$ corresponds to a given scale and resolution s and r , given by:

$$\frac{x - s}{r} = \frac{x_0 - s_0}{r_0}. \quad (11)$$

The scale and resolution estimates and their uncertainties are obtained from fitting the photon energy response model back to the simulation sample. The best fit values of the scale and resolution as derived from the photon energy response are used as references for generating a response model based on the $\mu\mu\gamma$ invariant mass and derived from the data.

To estimate the scale and resolution from the $\mu\mu\gamma$ invariant mass spectrum in data, we use a similar approach to the one discussed. There are however several important differences:

- In data the true energy response is not known, but if the scale is small a linear transformation can be written down relating the $\mu\mu\gamma$ invariant mass to the response and true energy. However, only the product of the response and true energy is known. Therefore we use the $\mu\mu\gamma$ invariant mass spectrum m instead of the photon energy response x to create a response model.
- The response model based on the $\mu\mu\gamma$ invariant mass spectrum is a sum of signal and background components whose relative fraction is floated in the fit. We use the simulation to build a kernel density estimate of the background component model. Only the signal component model depends on the parameters s and r .
- We use a different functional form for the invariant mass response transform introducing a linear dependence on the scale:

$$m \rightarrow m' = m + m \left\langle \frac{\partial \ln m}{\partial \ln E^\gamma} \right\rangle (s - s_0).$$

Here m' is the transformed $\mu\mu\gamma$ mass. The term in the angular brackets characterizes the linear dependence of the $\mu\mu\gamma$ mass on the photon energy.

- We introduce the dependence on the resolution through moment morphing, a technique for interpolating probability density functions, between a number of reference densities [37]. This method is based on the linearly transformed reference densities that have some reference mean expectation values and standard deviations. The linear transform is chosen such that the transformed densities reproduce the interpolated mean and standard deviation.

The reference densities are obtained from the simulation. Eq. 11 is used to smear the reconstructed photon energies to the desired resolution. The change in the photon energy is then propagated to the $\mu\mu\gamma$ invariant mass.

610 In Fig. 12 we show an example fit to the $\mu\mu\gamma$ mass in data and a comparison of the extracted
 611 photon energy scale in data and simulation with the true energy scale in simulation as a func-
 612 tion of photon transverse energy.

p_T^γ bin	MC true %	Data fit %
Barrel / Endcap		
$10 \leq p_T^\gamma \leq 12$	1.35 / 2.94	-1.40 / -1.84
$12 \leq p_T^\gamma \leq 15$	0.76 / 0.75	-1.85 / -0.87
$15 \leq p_T^\gamma \leq 20$	0.65 / 1.58	-1.22 / -1.68
$20 \leq p_T^\gamma \leq 50$	0.08 / 0.15	-1.22 / -0.15

Table 12: A summary of the derived photon energy scale estimates.

Given that the scale in data is estimated to be $s = s_{\text{data}}$, we calculate the corrected reconstructed energy E_{corr}^γ as:

$$E_{\text{corr}}^\gamma = E^\gamma(1 - s_{\text{data}}), \quad (12)$$

613 where E^γ is the uncorrected reconstructed energy. This also follows from Eq. 11 assuming
 614 $E_{\text{true}}^\gamma \approx E^\gamma / (1 + s_{\text{data}})$ and neglecting terms proportional to $O(s_{\text{data}}^2)$. In Table 12 we summarize
 615 both energy scale and resolution values used for the corrections in this analysis.

616 Eq. 11 is also used for the final correction of the simulation requiring perfect scale $s = 0$ and
 617 resolution equal to the one in data $r = r_{\text{data}}$. Substituting the uncorrected energy scale and
 618 resolution $s_0 = s_{\text{MC}}$ and $r_0 = r_{\text{MC}}$, a per-event nominal response x_0 gives the corrected and
 619 ‘smeared’ response x .